The effect of midnight temperature maximum winds on post-midnight equatorial spread F

Jonathan Krall[1], Dustin A Hickey[2], J.D. Huba[3], and PATRICK B DANDENAULT[4]

[1]Naval Research Laboratory
[2]United States Naval Research Laboratory
[3]Syntek Technologies
[4]Johns Hopkins University

November 24, 2022

Abstract

The SAMI3/ESF (Sami3 is also a model of the ionosphere/equatorial spread F) code is used to simulate the growth of equatorial plasma bubbles in the presence of a background wind field based on measured winds. The measured winds exhibit the well-known 'midnight temperature maximum' (MTM) pattern, in which an equatorward wind occurs simultaneously with a cessation in the zonal wind. The MTM is often preceded by strong equatorward winds (about 100 m/s). The circumstance where the MTM winds are symmetric across the equator is considered; here the meridional wind component in the southern hemisphere is the reverse of the northern meridional wind. The timing of the wind pattern relative to the imposition of a seed for the ESF instability is explored. We find that the simultaneous occurrence of a seed wave and a strong converging meridional wind pattern can produce post-midnight ESF. We further find that the seed wave and the sudden cessation of the zonal winds can also produce post-midnight ESF. The MENTAT (Magnetic mEridional NeuTrAl Thermospheric) code verifies the occurrence of converging meridional wind patterns such as those simulated here, based on ionosonde data. Results suggest that regional-scale wind measurements would aid in the prediction signal-disrupting ionospheric bubbles.

The effect of midnight temperature maximum winds on post-midnight equatorial spread F

J. Krall[1], D. Hickey[2], J.D. Huba[3], and P.B. Dandenault[4]

[1]Plasma Physics Division, Naval Research Laboratory, Washington, District of Columbia, USA
[2]Space Science Division, Naval Research Laboratory, Washington, District of Columbia, USA
[3]Syntek Technologies, Fairfax, VA, USA
[4]Applied Physics Laboratory, Johns Hopkins University, Laurel, MD, USA

Key Points:

- The timing of midnight temperature maximum winds affects the growth of post-midnight equatorial spread F
- Regional area wind measurements can aid in the prediction of ionospheric bubbles associated with the ESF instability
- Prediction of ESF bubbles requires wind measurements or wind predictions in both hemispheres

Corresponding author: Jonathan Krall, `jonathan.krall@nrl.navy.mil`

Abstract

The SAMI3/ESF (Sami3 is also a model of the ionosphere/equatorial spread *F*) code is used to simulate the growth of equatorial plasma bubbles in the presence of a background wind field based on measured winds. The measured winds exhibit the well-known 'midnight temperature maximum' (MTM) pattern, in which an equatorward wind occurs simultaneously with a cessation in the zonal wind. The MTM is often preceded by strong equatorward winds (about 100 m/s). The circumstance where the MTM winds are symmetric across the equator is considered; here the meridional wind component in the southern hemisphere is the reverse of the northern meridional wind. The timing of the wind pattern relative to the imposition of a seed for the ESF instability is explored. We find that the simultaneous occurrence of a seed wave and a strong converging meridional wind pattern can produce post-midnight ESF. We further find that the seed wave and the sudden cessation of the zonal winds can also produce post-midnight ESF. The MENTAT (Magnetic mEridional NeuTrAl Thermospheric) code verifies the occurrence of converging meridional wind patterns such as those simulated here, based on ionosonde data. Results suggest that regional-scale wind measurements would aid in the prediction signal-disrupting ionospheric bubbles.

Plain Language Summary

The local ionosphere often becomes unstable after dusk, with low-density 'bubbles' rising from the bottom of the ionosphere F layer upwards to altitudes of 1000 km or more. The jump in the local ionosphere density at the edges of these bubbles can disrupt signal transmission between Earth and space. The instability usually occurs after dusk but sometimes also occurs after midnight. We consider nighttime winds measured over an area covering most of the continental United States. The applicability of such measurements to prediction of bubbles is explored. The measured winds, which exhibit a phenomenon known as the midnight temperature maximum (MTM), are shown to enable post-midnight bubbles. Two separate mechanisms are considered: (1) a north/south converging meridional wind of the sort that often precedes the MTM and (2) the sudden cessation of the zonal wind that often occurs during the MTM. In each case, post-midnight ESF can occur if the timing between the winds and a 'seed' wave is optimum.

1 Introduction

The phenomenon known as equatorial spread *F* (ESF; Booker & Wells, 1938) is driven by the generalized Rayleigh-Taylor instability (Haerendel, 1974; Ossakow, 1981; Haerendel et al., 1992; Sultan, 1996). Previous studies show that zonal (Huba et al., 2009) and meridional (Krall et al., 2009) winds affect the growth of this instability. For example, a converging (diverging) meridional wind field can enhance (suppress) the instability (Huba & Krall, 2013). Because this instability produces equatorial plasma bubbles (EPBs) that affect communications (Kintner et al., 2007) and navigation (Sparks et al., 2004) signals, we are interested in both the occurrence and timing of ESF. In particular, while EPBs are typically observed shortly after dusk, they were recently found to occur after midnight and were observed quite often during the prolonged solar minimum of 2008-2009. Of particular interest is the finding that the seasonal and longitudinal dependencies differ from those of commonly observed post-sunset ESF (Heelis et al., 2010). For post-sunset ESF, the main cause of seasonal variation is understood to be the alignment of the terminator with the magnetic meridian (Tsunoda, 1985). For post-midnight ESF, the main cause of seasonal variation is not yet understood.

In this study we consider the thermospheric phenomenon known as the midnight temperature maximum (MTM). The MTM is an increase in temperature that occurs near local midnight. Modeling work suggests that the MTM should extend from low-latitudes into midlatitudes (Akmaev et al., 2009) and recent observations have supported this prediction (Hickey et al., 2014). The MTM has been observed in both the northern and summer hemisphere, away from the magnetic equator, as a rapidly-moving airglow enhancement associated with and following an increase in the thermosphere temperature (e.g. Spencer et al., 1979; Herrero & Spencer, 1982; M. J. Colerico et al., 2006; Hickey et al., 2018). Based on nighttime electron temperature measurements from the Jicamarca Radar Observatory, Bamgboye and McClure (1982) hypothesized that the MTM was a 'nighttime equatorial temperature bulge moving with the antisolar meridian.' This understanding of the MTM temperature and pressure bulge was supported by earlier radar studies by Behnke and Harper (1973) and Harper (1973), who demonstrated that a reversal of the meridional component of the thermospheric winds from equatorward to poleward forced the ionosphere downward, causing the brightness of the brightness wave (Friedman & Herrero, 1982). Recent modeling efforts have shown the importance of the semidiurnal, terdiurnal, and high order wave modes in the production of the MTM (Fesen, 1996; Akmaev et al., 2009). The MTM and its characteristic wind patterns (equatorward before the bulge passes; poleward after the bulge passes) tend to appear earlier near the equator and later at higher latitudes (Akmaev et al., 2009; Hickey et al., 2014).

Observations of this MTM wind pattern have been recently obtained over a large region of North America, using the North American Thermosphere Ionosphere Observing Network (NATION; Mesquita et al., 2018). The regional-scale NATION wind dataset shows rapid changes in wind strength and direction. The effect of such rapidly-varying winds on ESF has not been previously studied.

Below we will use these and other data to guide a study of the effect of MTM winds on the growth of EPBs. In so doing, we illustrate the value and the importance of such data for future studies. We submitted this manuscript to Space Weather specifically to illustrate the need for such wind measurements and to encourage decision makers to support further regional-scale observations.

We begin with a review of the NATION dataset that will be adapted for use in our simulations. In addition, we consider winds determined indirectly, using the Magnetic mEridional NeuTrAl Thermospheric (MENTAT) code. MENTAT determines meridional winds based on forward modeling and ionosonde data (Dandenault, 2018). Following discussion of NATION data, we briefly describe the high-resolution Sami3 is Another Model of the Ionosphere/Equatorial Spread F (SAMI3/ESF) regional 'wedge' model of the ionosphere. We present SAMI3/ESF simulation results showing that nighttime winds can enhance post-midnight ESF. We consider two mechanisms. First, a converging meridional wind can enhance ESF growth (Huba & Krall, 2013). The strong equatorward winds that often precede the MTM can form a converging wind pattern over the latitude range ($\pm 30°$) of these simulations. Note that this is not the same as the MTM-associated local converging wind analyzed by Mesquita et al. (2018) using these data. Second, the sudden decrease in zonal winds, which is correlated with the MTM, can also enhance ESF growth (Huba et al., 2009). In each case, ESF growth is sensitive to the timing of ESF-favoring winds relative to the imposition of a 'seed' perturbation at the beginning of the simulation.

2 Wind data

Winds were measured using the five Fabry-Perot interferometer (FPI) observatories that make up the NATION instrument (Mesquita et al., 2018). The wind data, some of which is adapted for use in our simulations and displayed in Figure 1, is centered on 38° N, 85° W and was measured beginning on 28 December 2013. Here, the wind vectors are denoted by 'wind flags' where the symbol is at the base of the the vector (i.e., they are not directional arrowheads). The latitude-longitude domain of Figure 1 encompasses the NATION domain, including points not in the NATION domain (e.g., the corners of the latitude-longitude box); missing information is filled in by using the nearest

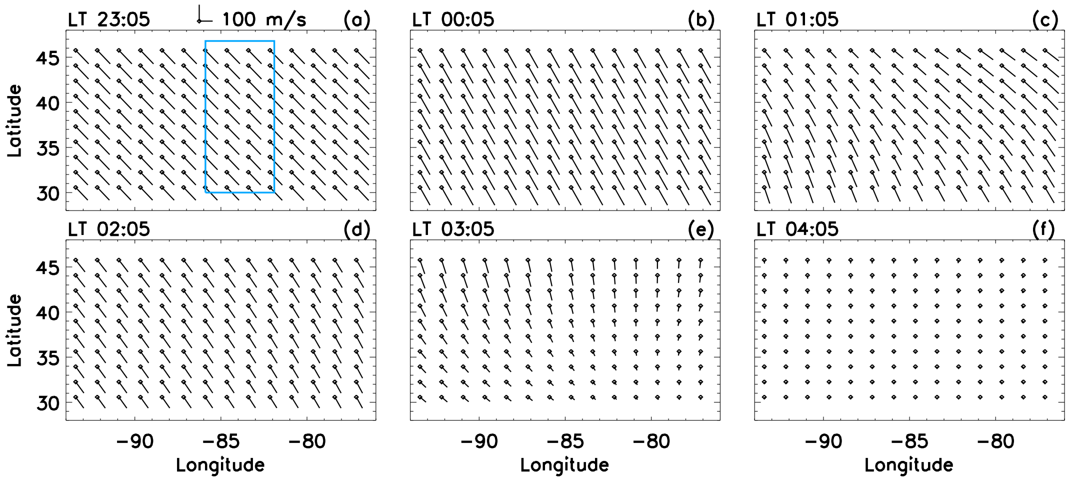

Figure 1. Regional wind field based on NATION measurements. At each point, the line indicates the direction of the wind *away* from the dot. Local time at longitude 85°W is indicated for each plot. The blue box indicates the subset region of the wind data used in the simulation.

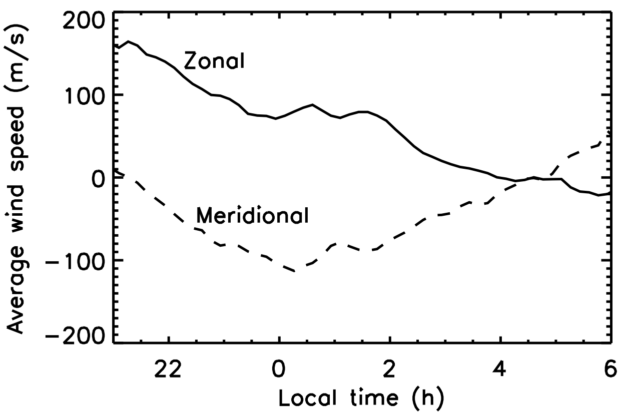

Figure 2. Average zonal and meridional wind speeds for the wind field of Figure 1

measured point. The subset of the latitude-longitude domain used in the SAMI3/ESF simulation, marked by a box in Figure 1a, is minimally affected by ‘filled in’ points.

Average zonal and meridional winds from Figure 1 are shown Figure 2. As described by Mesquita et al. (2018), measurements show a weak ‘secondary’ MTM at 2230 LT (0400 UT), followed by a strong meridional wind, peaking just past midnight local time, followed by the primary MTM at 0300 LT (0830 UT). The latter two features will be of interest in the simulations below. Between 0100 LT and 0600 LT, Figure 2 displays a characteristic MTM wind pattern, with equatorward winds before the MTM later becoming poleward, and zonal winds abating during the MTM. The primary MTM occurs relatively late, 3 hours after midnight. The NATION measurements illustrate the wake-wave nature of the MTM. This can be seen in Figure 1(c,) where the abatement of the zonal wind begins in the portion of the NATION wind field nearest to the equator before expanding to cover the entire field, Figure 1(d), and Figure 1(e), where a strong decrease in the meridional wind similarly begins in the equatorward half of the measured wind field.

The large, high-quality NATION dataset of Figure 1 is not ideally suited to a study of the effect of MTM winds on the growth of ESF. Specifically, the wind instruments in the NATION network (*NATION*, 2012) were all located above 35° N, too far from the equatorial region to affect this phenomenon. While EPBs commonly extend north and south along field lines to magnetic latitudes of ±30° or more, simulations suggest that the winds that affect ESF growth are located at latitudes of 5 to 15° north and south of the magnetic equator (e.g. Krall et al., 2013, Fig. 1). Winds showing the MTM pattern similar to that of Figure 2 are seen at a range of latitudes with the pattern occurring later in local time at higher latitudes (Friedman & Herrero, 1982; Akmaev et al., 2009). It is therefore reasonable to use winds at the NATION latitude as a proxy for winds at lower latitudes.

Ideally, for the study (or prediction) of the effect of winds on ESF, we would have a NATION-like observing network 10° north of the magnetic equator and another at 10° south of the magnetic equator. To obtain winds in the southern hemisphere for the present study, we will consider a variety of approaches.

3 SAMI3/ESF Model

We used the SAMI3/ESF 'wedge' model (Huba et al., 2008) of the ionosphere for this study. SAMI3/ESF is a version of the global SAMI3 ionosphere model that simulates a narrow wedge, in longitude, of the global ionosphere. In this case the simulation has width 4 degrees and maximum altitude 2400 km. The SAMI3 grid is arranged along field lines; the highest altitude model field line in this case extends to magnetic latitudes of about ±30°. For convenience, we approximate the geomagnetic field to be a centered dipole field, such that the geographic and magnetic latitudes are the same. We place the wedge at longitude 0°, so local and universal times are approximately the same. The model ionosphere has periodic boundary conditions in longitude, such that ESF bubbles that exit at longitude 4° re-enter the simulation at longitude 0°.

For these model runs, we set the $F_{10.7}$ EUV index and its 80-day average to 130, indicating moderate solar activity. We set the day of year to 80 (spring equinox). We begin each simulation at 23:03 UT. This is long after the ionosphere has been lifted by the pre-reversal enhancement of the wind-driven electric field; by this time the ionosphere has fallen to lower altitudes. We impose random perturbations localized to a region of width 0.5° in longitude near altitude 300 km. Perturbations can be as large as 15% of the background density and are imposed along the entirety of each model field line.

The adaptation of the NATION winds to the SAMI3/ESF grid is shown in Figure 3. Note that we use only zonal and meridional winds in the simulation. Because vertical winds outside of the NATION region are not known, and empirical models are not well-developed, vertical winds in SAMI3/ESF are set to zero. To investigate the effect of the measured wind field on the model ionosphere, we shift the data by 22 degrees in latitude, moving a subset of the measured wind field, indicated by a blue box in Figure 3(a) into the northern part of the model ionosphere, Figure 3(d). The measured wind field is also shifted in longitude. For this reason, we refer only to local time in Figures 1-3 and below. Because the MTM begins near the anti-solar point, expanding northward (and southward) versus time, shifting the wind field to lower latitude without changing the time coordinate is equivalent to assuming the MTM occurred later in time than it actually did by about an hour. This is much less than the observed night-to-night variability in MTM timing.

Clearly the measured winds cover only a fraction of the simulation domain of Figure 3(d-f). North of this region, the model winds are set equal to the nearest (in latitude and longitude) measured wind value. To obtain winds in the southern hemisphere, we consider the case in which winds in the south are approximately the mirror of winds

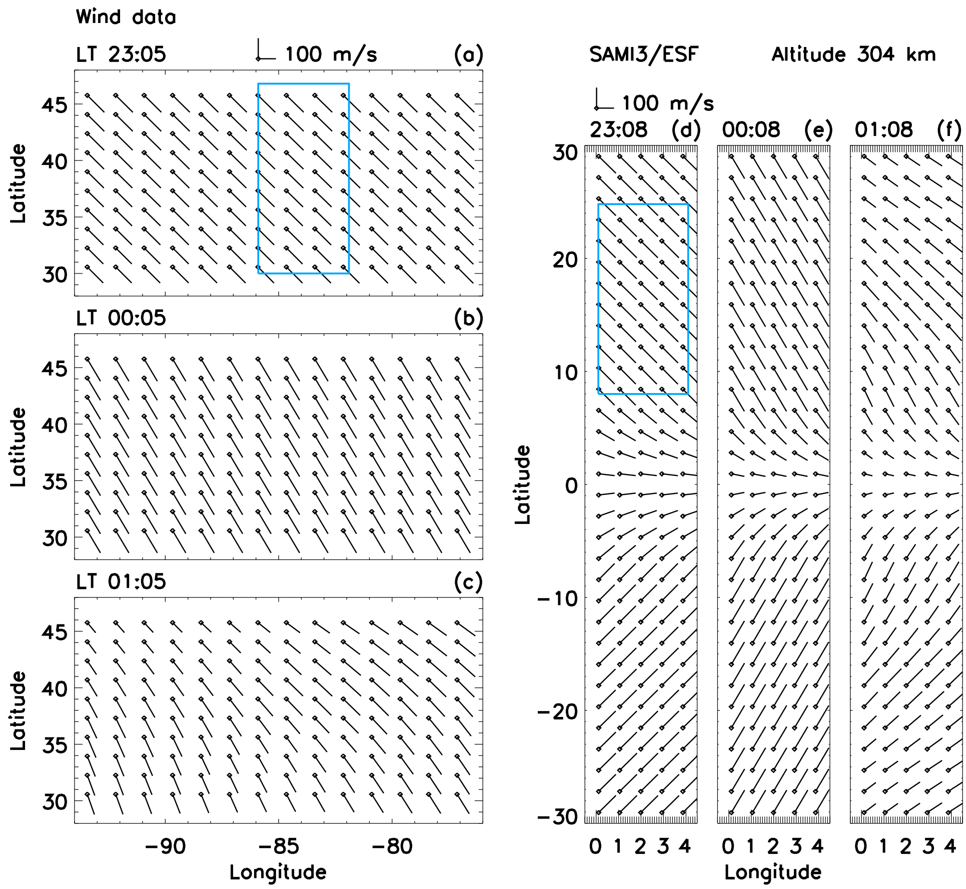

Figure 3. a-c: measured wind direction at various times (repeated from Figure 1). d-f: Wind direction on the SAMI3/ESF grid. At each point, the line indicates the direction of the wind *away* from the dot. The blue box indicates the subset (in longitude and latitude) of the wind data used in the simulation.

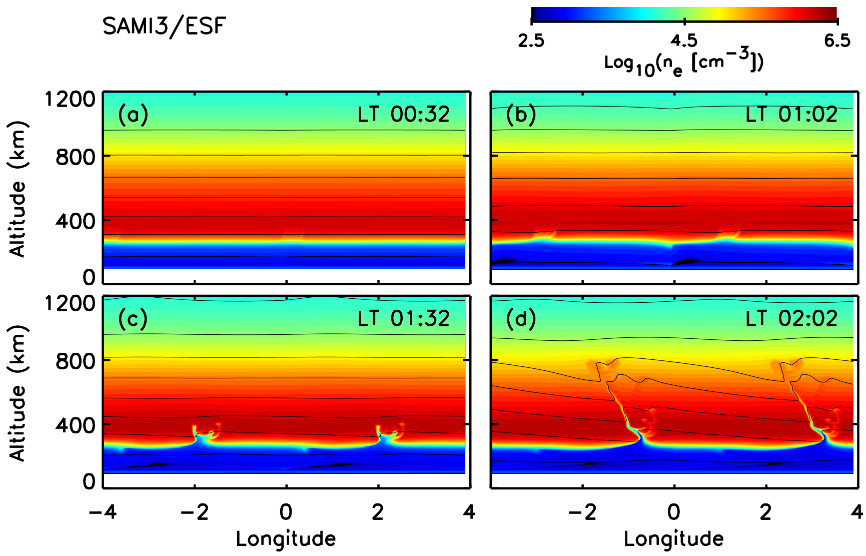

Figure 4. Color contours of the log of the electron density are plotted versus longitude and altitude at the magnetic equator at four different times. Also shown are contour lines, indicating the electric potential. Initially, the electric field is dominated by dielectric fields driven by the zonal wind. Two longitudinal periods of the periodic grid are shown. This is the result with winds as shown in Figure 3.

in the north, with the zonal wind set equal to the corresponding value in the north and the meridional wind being opposite the corresponding value in the north. Between -8° and 8°, winds are linearly interpolated, based on nearest measured values. Observations by Herrero and Spencer (1982) show that during equinox months (when the antisolar point is near the geographic equator) the MTM is generally symmetric about the geographic equator.

4 Results

Figure 4 shows color contours of the log of the electron density plotted versus longitude and altitude at the magnetic equator plotted at four different times. The growth of EPBs is evident, but slow. Bubbles reach altitude 800 km at 02:02 local time, 3 hours after the beginning of the simulation. Also shown in Figure 4 are contour lines indicating the electric potential. Horizontal potential lines indicate the zonal-wind-driven dielectric field that 'blows' the bubbles eastward. Vertical deflections of the contour lines indicate the electric field inside each rising bubble; a sharp deflection indicates a strong electric field.

Because the timing of the MTM wind pattern shows 'significant day-to-day variability' (M. Colerico et al., 1996), we performed simulations in which we varied the timing of the winds of Figure 3 relative to the beginning of the simulation, when the initial perturbation is imposed. For example, Figure 5 shows the growth of EPBs for a case in which the wind pattern of Figure 3 occurs one hour earlier. Here the strongest converging meridional winds (Figure 3e) occur at about 23:00 LT, near the beginning of the simulation. As a result, the EBPs grow faster than in the previous case, with EPBs exceeding 1000 km altitude at 01:03 LT, 2 hours after the beginning of the simulation. Huba

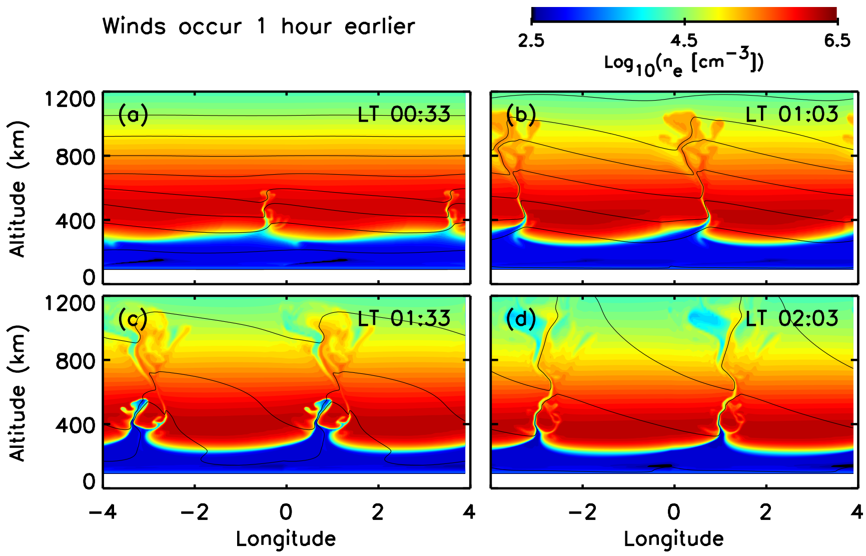

Figure 5. Same as Figure 4, but with MTM winds occurring one hour earlier.

and Krall (2013) showed that a large-scale converging meridional wind enhances ESF growth rates.

Further simulations showed that post-midnight ESF could also be enhanced by a combination of a weak converging meridional wind and a near-zero zonal wind. Observers have identified the abatement of zonal winds as a signature of the MTM (Wharton et al., 1984; Herrero et al., 1985). In Figure 6 we show measured winds (panels a-c) and corresponding model winds (panels d-f) for a case where we consider the MTM winds of Figures 1 and 3 to have occurred 4 hours earlier in local time. In this case the simulation begins with a very weak zonal wind and a moderate converging meridional wind, Figure 6(d). The winds then fall almost entirely to zero, Figure 6(e), before beginning to reverse, Figure 6(f). Huba et al. (2009) showed that zonal winds reduce ESF growth rates. Figure 7 shows the result. Initial growth, Figure 7(a), 90 minutes after the beginning of the simulation, is faster than in the other two cases. However, with the reversal of the meridional winds, beginning about 2 hours into the simulation, the bubbles stop rising, Figure 7(c,d).

5 Discussion

As noted above, theoretical analysis of the effects of winds on ESF shows that a converging meridional wind pattern is destabilizing (Huba & Krall, 2013). While this pattern is clear in Figure 3(d-f), with the strongest converging wind occurring just after midnight, Huba and Krall (2013) shows that the growth rate depends on the gradient of the wind versus latitude; a converging wind that is everywhere northward (or southward) is similarly unstable. It should be noted that, while the MTM is typically preceded by an equatorward wind, we are not aware of a correlation between the strength of such winds and MTM occurrence.

Earlier analysis by Huba et al. (2009) implied that reduced zonal winds also enhance ESF growth. In the case where the zonal wind is nearly zero Figure 6(d), a relatively moderate converging meridional wind can also enhance post-midnight ESF. These results are consistent with these previous analytical results, with the strongest growth

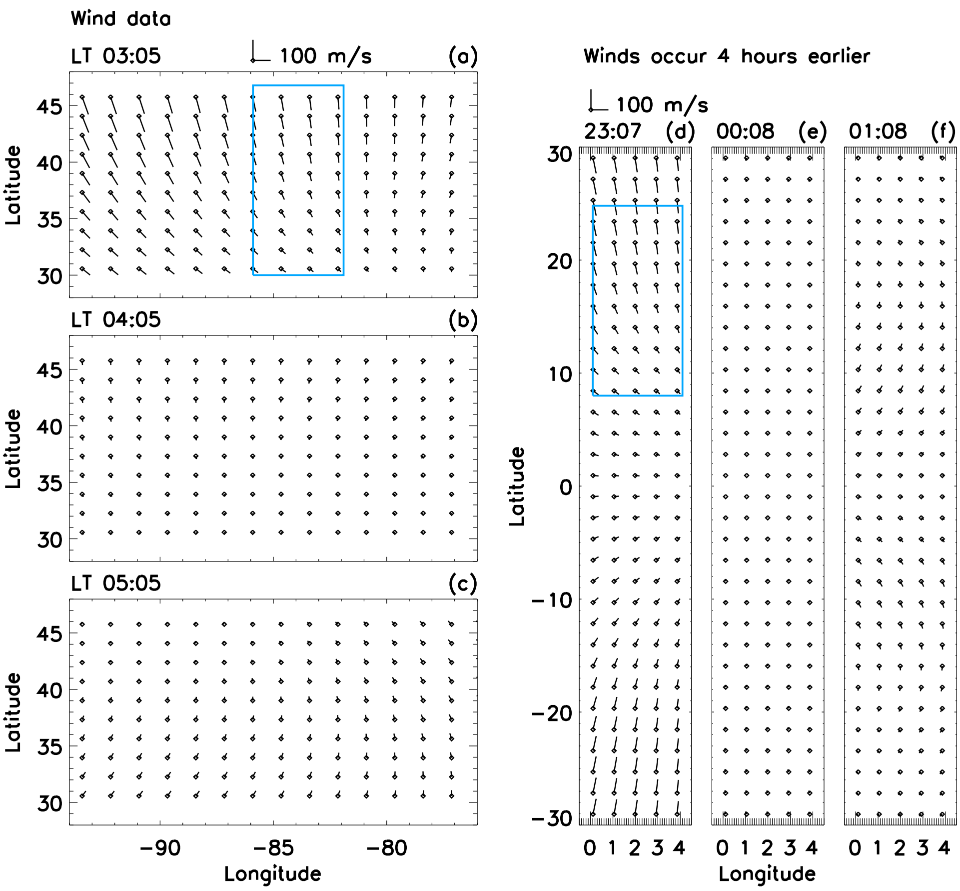

Figure 6. a-c: measured wind direction at various times. d-f: Wind direction on the SAMI3/ESF grid for a case where SAMI3/ESF winds are based on measured winds, but shifted by 4 hours. At each point, the line indicates the direction of the wind *away* from the dot.

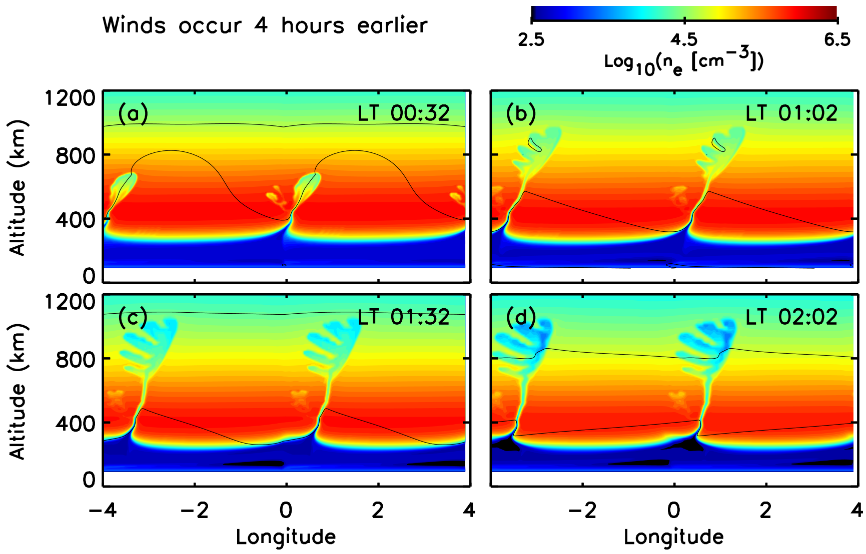

Figure 7. Same as Figure 4, but with MTM winds occurring four hours earlier.

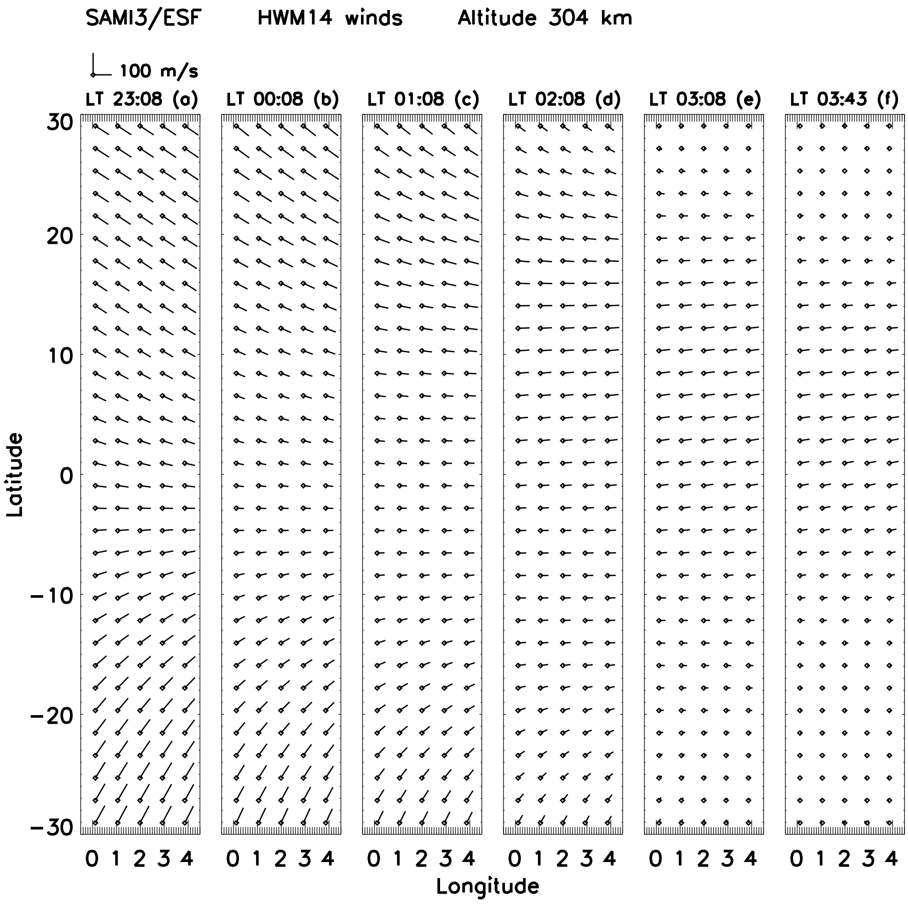

Figure 8. HWM14 winds on the SAMI3/ESF grid at various times for day 80 and $F_{10.7} = F_{10.7a} = 130$. At each point, the line indicates the direction of the wind *away* from the dot.

found in the case with the strongest gradient (Figure 5) or with the weakest zonal wind (Figure 7) at the beginning of the simulation, when the seed is imposed.

5.1 MTM winds and post-midnight ESF

As noted above, Heelis et al. (2010) reports that post-midnight ESF has a seasonal dependence that differs from the usual post-sunset ESF. In particular, post-midnight ESF occurs most often in summer at longitudes 0-60°E and in winter at longitudes 150-90°W. In the case of MTM, Herrero and Spencer (1982) analyzed Atmosphere Explorer E satellite data, finding that, as with post-midnight ESF, the MTM is strongest in summer and winter, with the smaller peak being in winter. However, MTM data have not been analyzed to determine longitudinal dependence. Noting a correlation between the occurrence of the MTM and post-midnight ESF in data collected at Waltair (17.7°N, 83.3°E) Niranjan et al. (2003) suggest a connection. In particular, they suggest that meridional winds might drive the F layer upward, increasing the ESF growth rate.

The increase in the ESF growth rate that occurs if the F layer is lifted is not the same as the increase in the ESF growth rate caused by the presence of a converging meridional wind. In fact, because we initiated these simulations based on a SAMI2 run with HWM14 winds, we may be missing the uplift of the model ionosphere prior to the beginning of the SAMI3/ESF simulation. Once the SAMI3/ESF simulation commences, both effects come into play. This uplift is not visible in Figures 4, 5 and 7, which are plotted at the equator. Additional plots (not shown) indicate an uplift of over 50 meters at $\pm 10°$ latitude during the first hour for the simulation of Figure 5.

Both Niranjan et al. (2003) and Heelis et al. (2010) find a reduction in post-midnight ESF occurrence as the the solar cycle increases away from solar minimum. Our present study does not provide a ready explanation for this effect. For example, when we repeat the simulation of Figure 4 with $F_{10.7} = F_{10.7a} = 80$ (instead of 130) in both the SAMI2-computed initial conditions and the SAMI3/ESF simulation, results showed ESF growth very similar to, but slightly weaker than, that of Figure 4.

5.2 Model MTM winds

To obtain the winds of Figures 3 and 6, we assumed that the MTM winds of the NATION dataset are representative of MTM winds at latitudes closer to the equator and that north-south symmetry is a common occurrence. We address the latter assumption in Figure 8. Here winds from the Horizontal Wind Model (HWM14; Drob et al., 2015) are shown on the SAMI3/ESF grid for the same parameters (day 80, $F_{10.7} = F_{10.7a} = 130$) as in Figures 4, 5 and 7 above. In Figure 8(a,b) we see a converging wind pattern similar to Figure 3(e,f), but with weaker winds. When the simulation of Figure 4 is repeated using the Figure 8 winds, ESF grows more slowly.

HWM14 is an empirical model that computes typical zonal and meridional winds for a specified day and time. Because the MTM occurs only some of the time, we speculate that nights with a strong MTM wind pattern are included, along with nights with no MTM, in the data that are the basis for the HWM14 model. For example, the NATION instrument showed that, 'out of a total number of 846 analyzed nights, 44% were inconclusive, 43% had no MTM peaks, and 13% had the presence of the MTM in the temperature data' (Mesquita et al., 2018). Hence, a relatively weak MTM-like wind pattern is found in HWM14, including the reversal from equatorward to poleward (not shown; it occurs after 04:30 LT), but without the wake-like structure in the abatement of the zonal wind.

We now consider the imposition of north-south symmetry in the MTM wind pattern of Figure 3. In addition to being evident in the HWM14 winds for day 80, Figure 8, the corresponding symmetry in the thermosphere temperature pattern was observed by Herrero and Spencer (1982, Figs. 5 and 7) using satellite measurements. These results suggest that our model winds are realistic, but with a caveat. The winds of Figure 3 are symmetric, as might be expected at an equinox but also relatively strong, as might be expected at a solstice.

5.3 MENTAT meridional winds

The MENTAT code of Dandenault (2018) provides another approach to determining thermosphere winds. MENTAT determines meridional winds based on forward modeling and ionosonde data, but with a significant caveat. In MENTAT, winds in a single-field-line ionosphere model are adjusted to bring the model ionosphere in line with observations at a specified longitude and latitude. However, as winds are adjusted, only the direct effect of the adjusted winds on the ionosphere is included. By 'direct effect' we refer to the tendency of meridional winds to push ionosphere plasma up or down field lines. In MENTAT, adjusted winds do not alter the global wind-driven dynamo **E** field.

With that important caveat duly noted, we used MENTAT to compute winds at longitude -85° and latitudes -30, -25, -20, -15,-10,-5, 5, 10, 15, 20, 25, and 30°. Hourly meridional wind values were obtained for 2012, 2013, and 2014. For zonal wind values, we used HWM14.

For each day of our MENTAT results, we computed the the meridional wind gradient in the hours near midnight, finding the strongest gradients nearer to the solstices than to the equinoxes. This is consistent with Herrero and Spencer (1982), who find the strongest temperature maxima at the solstices. Overall, we found that winds similar to that of Figure 8 were common, while winds similar to that of Figure 3 were less common. Specifically, MENTAT winds usually had a meridional wind gradient smaller in magnitude than that of Figure 3(e).

One of the strongest MTM wind patterns found in our MENTAT survey, shown in Figure 9, is similar to the winds of Figure 3. When we repeated the simulation of Figure 4 with these MENTAT winds used in place of the Figure 3 winds, ESF grew faster than in Figure 4 but slower than in Figure 5. We conclude that the winds shown in Figure 3 are realistic.

Note that our example wind fields, Figures 3, 8 and 9, are not comprehensively representative of MTM winds. In particular, MENTAT often produced winds with both a strong meridional wind gradient and an overall northward (or southward) wind direction. That is, the converging and constant meridional wind components were often comparable.

6 Conclusions

The SAMI3/ESF code was used to simulate the growth of equatorial plasma bubbles in the presence of an MTM wind field based on measured winds. We focused on two specific characteristics of MTM winds. First, we consider the equatorward wind that typically precedes the MTM. Second, we consider the abatement of the zonal wind that is observed at the time of the MTM. These nighttime winds were shown to support the growth of post-midnight ESF, with bubbles typically rising above the F layer within 2 hours of simulated time.

This result was found for cases with a strong converging meridional wind gradient (Figure 5) *or* with a moderate gradient and a very weak ($<$ 20 m/s) zonal wind (Figure 7). The growth of ESF, however, was sensitive to the timing of the winds relative to the imposition of the density perturbation that seeds the instability. Once the meridional wind reverses direction, the instability stops growing (Figure 5c,d). These results are consistent with prior analyses of the generalized Rayleigh-Taylor instability. Specif-

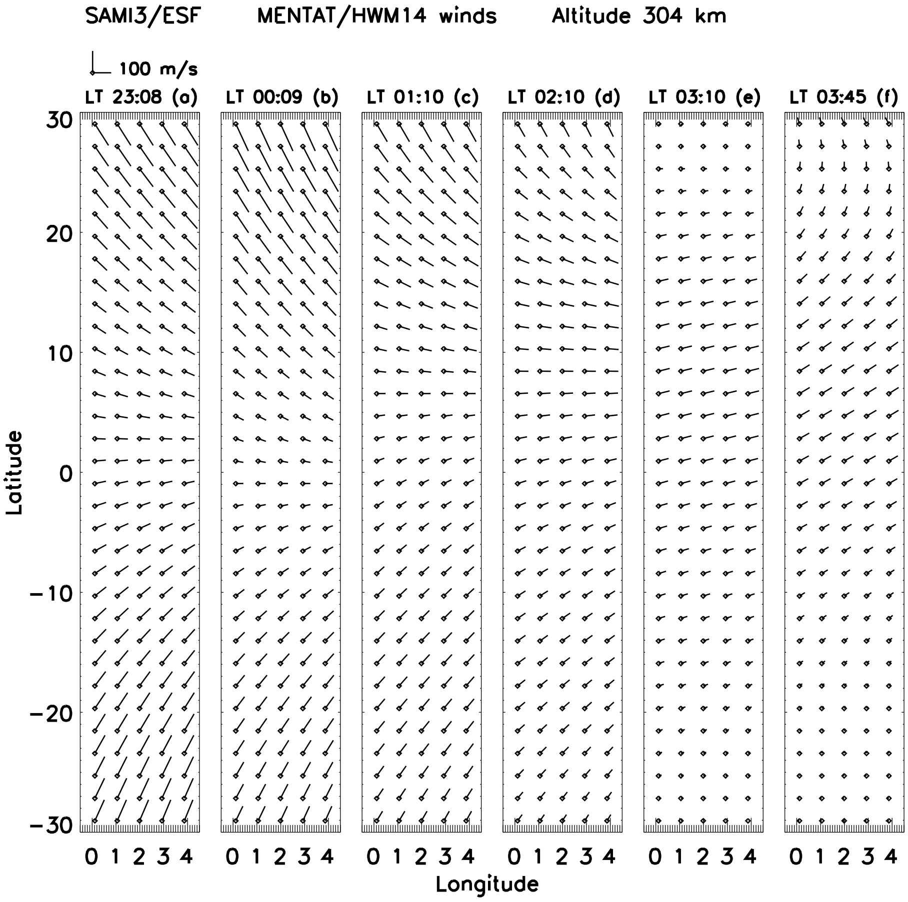

Figure 9. MENTAT meridional winds and HWM14 zonal winds on the SAMI3/ESF grid at various times for 1 December 2013 (day 335). At each point, the line indicates the direction of the wind *away* from the dot.

ically, a converging (diverging) meridional wind component is destabilizing (stabilizing) (Huba & Krall, 2013) and a reduced zonal wind increases growth rates (Huba et al., 2009).

As a check on our results, we computed meridional winds at this same longitude (85° W) using the MENTAT code, which determines meridional winds based on ionosonde data and forward modeling. Beyond a finding that the winds shown in Figures 3 and 6 are realistic, it is difficult to draw strong conclusions from our MENTAT study. The idea that forward modeling of the ionosphere could provide wind information over a large region, such as the 4° longitude by 60° latitude region simulated in SAMI3/ESF, is appealing. However, the MENTAT code provides only meridional winds and has not yet been validated on such a large scale. To our knowledge, forward modeling on a global scale, which would give both meridional and zonal winds, is not yet numerically feasible.

These results suggest that regional-scale wind measurements, such as from the NATION instrument, could be applied to the nowcasting of ESF, EPBs, and resulting scintillation. However, such measurements would need to cover latitude ranges 5 to 15° north and south of the magnetic equator.

To this final point, we note that the NASA Ionospheric Connection Explorer (ICON; Immel et al., 2018) was launched on October 10, 2019 and is measuring meridional and zonal neutral wind measurements with the Michelson Interferometer for Global High-resolution Thermospheric Imaging (MIGHTI) instrument. The MIGHTI nighttime observations span the altitude ranges $\sim$ 90 - 110 km and $\sim$ 210 - 300 km in the low-latitude ionosphere. Thus, ICON will provide meridional wind measurements to more fully explore the relationship between the MTM and post-midnight ESF.

Acknowledgments

This research was supported by NRL Base Funds and NASA Heliophysics Supporting Research award 80HQTR18T0077. ICON is supported by NASA's Explorers Program through contracts NNG12FA45C and NNG12FA42I. We thank Douglas P. Drob of the NRL Space Science Division for helpful comments. The NATION data and MENTAT output used here, along with numerical information associated with each of the SAMI3/ESF figures, are available at https://doi.org/10.5281/zenodo.4444085.

References

Akmaev, R. A., Wu, F., Fuller-Rowell, T. J., & Wang, H. (2009). Midnight temperature maximum (MTM) in whole atmosphere model (WAM) simulations. *Geophysical Research Letters*, *36*(7), L07108. doi: https://doi.org/10.1029/2009GL037759

Bamgboye, D. K., & McClure, J. P. (1982). Seasonal variation in the occurrence time of the equatorial midnight temperature bulge. *Geophysical Research Letters*, *9*(4), 457–460. doi: https://doi.org/10.1029/GL009i004p00457

Behnke, R. A., & Harper, R. M. (1973). Vector measurements of F region ion transport at Arecibo. *Journal of Geophysical Research*, *78*(34), 8222–8234. doi: https://doi.org/10.1029/JA078i034p08222

Booker, H. G., & Wells, H. W. (1938). Scattering of radio waves by the F-region of the ionosphere. *Terrestrial Magnetism and Atmospheric Electricity*, *43*(3), 249–256. doi: https://doi.org/10.1029/TE043i003p00249

Colerico, M., Mendillo, M., Nottingham, D., Baumgardner, J., Meriwether, J., Mirick, J., … Biondi, M. A. (1996). Coordinated measurements of F region dynamics related to the thermospheric midnight temperature maximum. *Journal of Geophysical Research: Space Physics*, *101*(A12), 26783–26793. doi: https://doi.org/10.1029/96JA02337

Colerico, M. J., Mendillo, M., Fesen, C. G., & Meriwether, J. (2006). Comparative investigations of equatorial electrodynamics and low-to-mid latitude coupling of the thermosphere-ionosphere system. *Annales Geophysicae*, *24*(2), 503–513. doi: https://doi.org/10.5194/angeo-24-503-2006

Dandenault, P. B. (2018). MENTAT: A new wind model for Earth's thermosphere. *Journal of Geophysical Research: Space Physics*, *123*(8), 7124–7147. doi: https://doi.org/10.1029/2018JA025551

Drob, D. P., Emmert, J. T., Meriwether, J. W., Makela, J. J., Doornbos, E., Conde, M., ... Klenzing, J. H. (2015). An update to the Horizontal Wind Model (HWM): The quiet time thermosphere. *Earth and Space Science*, *2*(7), 301–319. doi: https://doi.org/10.1002/2014EA000089

Fesen, C. G. (1996). Simulations of the low-latitude midnight temperature maximum. *Journal of Geophysical Research: Space Physics*, *101*(A12), 26863-26874. doi: https://doi.org/10.1029/96JA01823

Friedman, J. F., & Herrero, F. A. (1982). Fabry-Perot interferometer measurements of thermospheric neutral wind gradients and reversals at Arecibo. *Geophysical Research Letters*, *9*(7), 785–788. doi: https://doi.org/10.1029/GL009i007p00785

Haerendel, G. (1974). Theory of equatorial spread *F*. *Max-Planck Inst. für Extraterr. Phys.*. (unpublished report)

Haerendel, G., Eccles, J. V., & Çakir, S. (1992). Theory for modeling the equatorial evening ionosphere and the origin of the shear in the horizontal plasma flow. *Journal of Geophysical Research: Space Physics*, *97*(A2), 1209–1223. doi: https://doi.org/10.1029/91JA02226

Harper, R. (1973). Nighttime meridional neutral winds near 350 km at low to mid-latitudes. *Journal of Atmospheric and Terrestrial Physics*, *35*(11), 2023–2034. doi: https://doi.org/10.1016/0021-9169(73)90116-5

Heelis, R. A., Stoneback, R., Earle, G. D., Haaser, R. A., & Abdu, M. A. (2010). Medium-scale equatorial plasma irregularities observed by Coupled Ion-Neutral Dynamics Investigation sensors aboard the Communication Navigation Outage Forecast System in a prolonged solar minimum. *Journal of Geophysical Research: Space Physics*, *115*(A10). doi: https://doi.org/10.1029/2010JA015596

Herrero, F. A., Mayr, H. G., Spencer, N. W., Hedin, A. E., & Fejer, B. G. (1985). Interaction of zonal winds with the equatorial midnight pressure bulge in the Earth's thermosphere: Empirical check of momentum balance. *Geophysical Research Letters*, *12*(8), 491–494. doi: https://doi.org/10.1029/GL012i008p00491

Herrero, F. A., & Spencer, N. W. (1982). On the horizontal distribution of the equatorial thermospheric midnight temperature maximum and its seasonal variation. *Geophysical Research Letters*, *9*(10), 1179–1182. doi: https://doi.org/10.1029/GL009i010p01179

Hickey, D. A., Martinis, C. R., Erickson, P. J., Goncharenko, L. P., Meriwether, J. W., Mesquita, R., ... Wright, A. (2014). New radar observations of temporal and spatial dynamics of the midnight temperature maximum at low latitude and midlatitude. *Journal of Geophysical Research: Space Physics*, *119*(12), 10,499-10,506. doi: https://doi.org/10.1002/2014JA020719

Hickey, D. A., Martinis, C. R., Mendillo, M., Baumgardner, J., Wroten, J., & Milla, M. (2018). Simultaneous 6300 å airglow and radar observations of ionospheric irregularities and dynamics at the geomagnetic equator. *Annales Geophysicae*, *36*(2), 473–487. doi: https://doi.org/10.5194/angeo-36-473-2018

Huba, J. D., Joyce, G., & Krall, J. (2008). Three-dimensional equatorial spread *F* modeling. *Geophysical Research Letters*, *35*. doi: https://doi.org/10.1029/2008GL033509

Huba, J. D., & Krall, J. (2013). Impact of meridional winds on equatorial spread *F*: Revisited. *Geophysical Research Letters*, *40*(7), 1268–1272. doi: https://doi

.org/10.1002/grl.50292

Huba, J. D., Ossakow, S. L., Joyce, G., Krall, J., & England, S. L. (2009). Three-dimensional equatorial spread F modeling: Zonal neutral wind effects. *Geophysical Research Letters*, *36*(19). doi: https://doi.org/10.1029/2009GL040284

Immel, T. J., England, S. L., Mende, S. B., Heelis, R. A., Englert, C. R., Edelstein, J., . . . Sirk, M. M. (2018). The Ionospheric Connection Explorer Mission: Mission goals and design. *Space Science Reviews*, *214*(13). doi: https://doi.org/10.1007/s11214-017-0449-2

Kintner, P. M., Ledvina, B. M., & de Paula, E. R. (2007). GPS and ionospheric scintillations. *Space Weather*, *5*(9). doi: https://doi.org/10.1029/2006SW000260

Krall, J., Huba, J. D., Joyce, G., & Hei, M. (2013). Simulation of the seeding of equatorial spread F by circular gravity waves. *Geophysical Research Letters*, *40*(1), 1–5. doi: https://doi.org/10.1029/2012GL054022

Krall, J., Huba, J. D., Joyce, G., & Zalesak, S. T. (2009). Three-dimensional simulation of equatorial spread-F with meridional wind effects. *Annales Geophysicae*, *27*(5), 1821–1830. doi: https://doi.org/10.5194/angeo-27-1821-2009

Mesquita, R. L. A., Meriwether, J. W., Makela, J. J., Fisher, D. J., Harding, B. J., Sanders, S. C., . . . Ridley, A. J. (2018). New results on the mid-latitude midnight temperature maximum. *Annales Geophysicae*, *36*(2), 541–553. doi: https://doi.org/10.5194/angeo-36-541-2018

NATION. (2012). `http://airglow.ece.illinois.edu/Research/NATION`. (Accessed: 2021-01-30)

Niranjan, K., Brahmanandam, P. S., Ramakrishna Rao, P., Uma, G., Prasad, D. S. V. V. D., & Rama Rao, P. V. S. (2003). Post midnight spread-F occurrence over Waltair (17.7° N, 83.3° E) during low and ascending phases of solar activity. *Annales Geophysicae*, *21*(3), 745—750. doi: https://doi.org/10.5194/angeo-21-745-2003

Ossakow, S. L. (1981). Spread-F theories-a review. *Journal of Atmospheric and Terrestrial Physics*, *43*(5-6), 437–452. (Equatorial Aeronomy - I) doi: https://doi.org/10.1016/0021-9169(81)90107-0

Sparks, L., Komjathy, A., & Mannucci, A. J. (2004). Sudden ionospheric delay decorrelation and its impact on the Wide Area Augmentation System (WAAS). *Radio Science*, *39*(1). doi: https://doi.org/10.1029/2002RS002845

Spencer, N. W., Carignan, G. R., Mayr, H. G., Niemann, H. B., Theis, R. F., & Wharton, L. E. (1979). The midnight temperature maximum in the Earth's equatorial thermosphere. *Geophysical Research Letters*, *6*(6), 444–446. doi: https://doi.org/10.1029/GL006i006p00444

Sultan, P. J. (1996). Linear theory and modeling of the Rayleigh-Taylor instability leading to the occurrence of equatorial spread F. *Journal of Geophysical Research: Space Physics*, *101*(A12), 26875–26891. doi: https://doi.org/10.1029/96JA00682

Tsunoda, R. T. (1985). Control of the seasonal and longitudinal occurrence of equatorial scintillations by the longitudinal gradient in integrated E region Pedersen conductivity. *Journal of Geophysical Research: Space Physics*, *90*(A1), 447–456. doi: https://doi.org/10.1029/JA090iA01p00447

Wharton, L. E., Spencer, N. W., & Mayr, H. G. (1984). The earth's thermospheric superrotation from dynamics explorer 2. *Geophysical Research Letters*, *11*(5), 531–533. doi: https://doi.org/10.1029/GL011i005p00531

Figure 1.

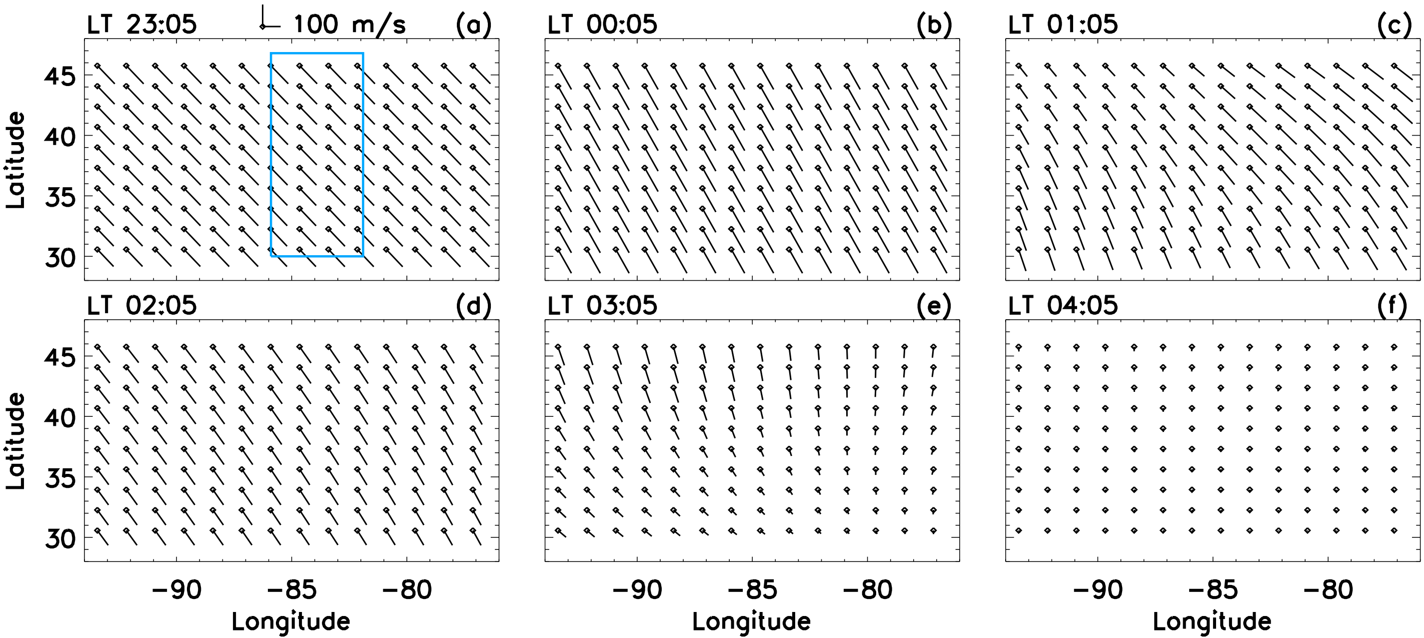

LT 23:05
100 m/s
(a)
LT 00:05
(b)
LT 01:05
(c)
LT 02:05
(d)
LT 03:05
(e)
LT 04:05
(f)
Latitude
45
40
35
30
−90
−85
−80
Longitude

Figure 2.

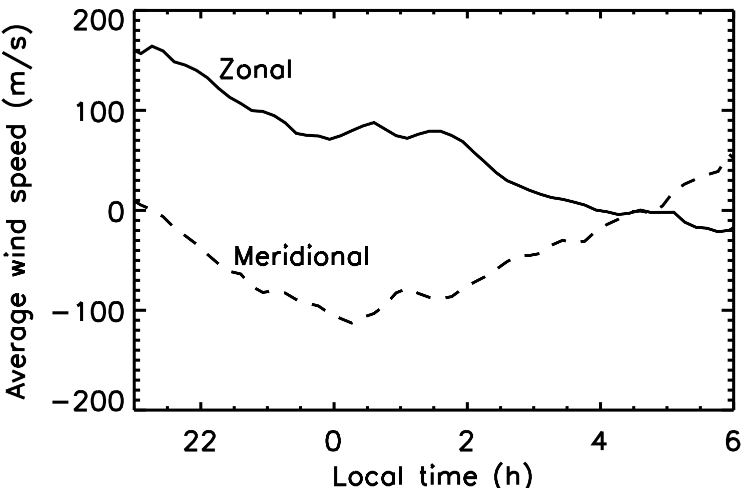

Zonal
Meridional
200
100
0
−100
−200
Average wind speed (m/s)
22
0
2
4
6
Local time (h)

Figure 3.

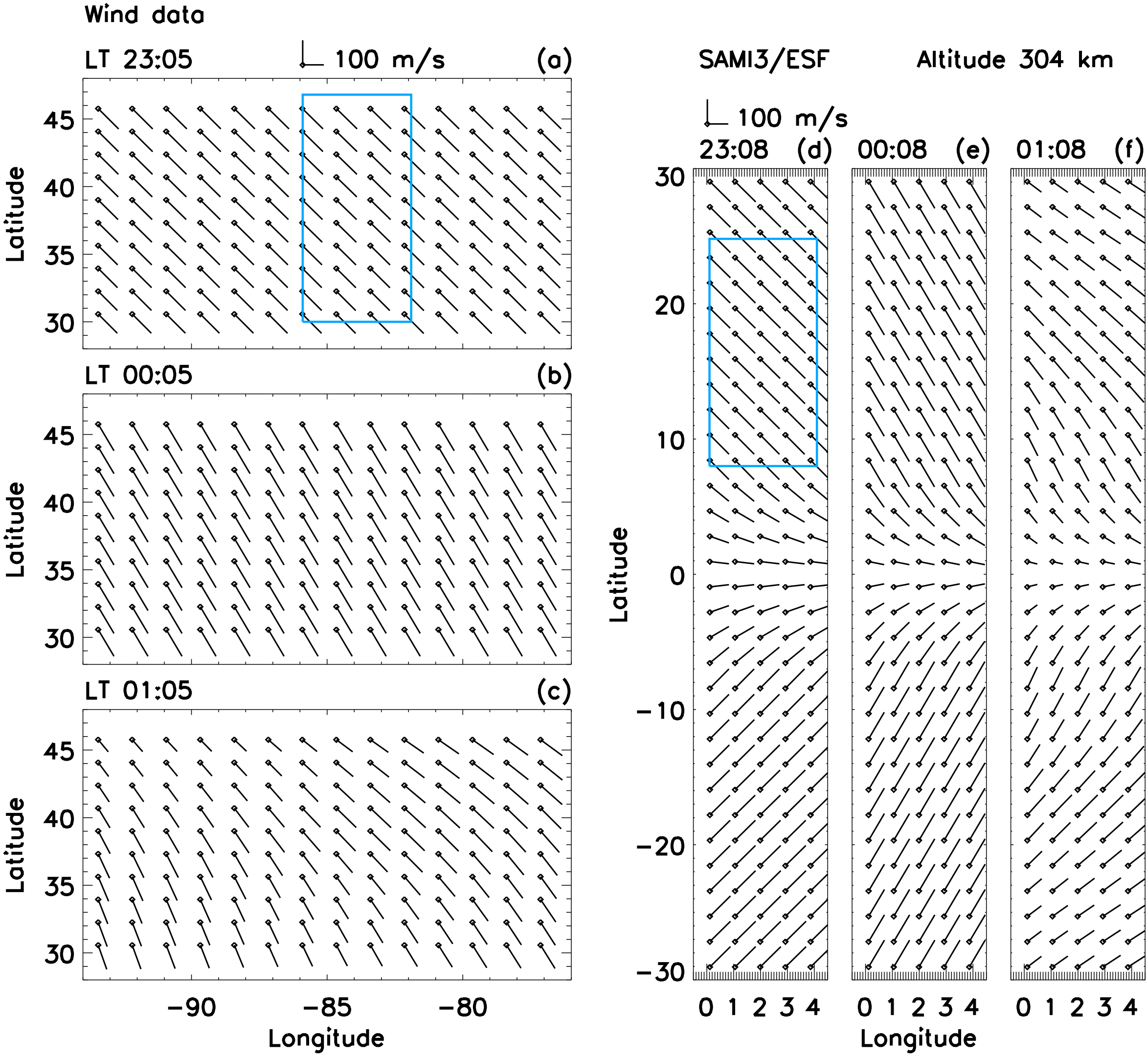
Wind data
LT 23:05
100 m/s
(a)
LT 00:05
(b)
LT 01:05
(c)
Latitude
Longitude
SAMI3/ESF
Altitude 304 km
100 m/s
23:08
(d)
00:08
(e)
01:08
(f)
Latitude
Longitude

Figure 4.

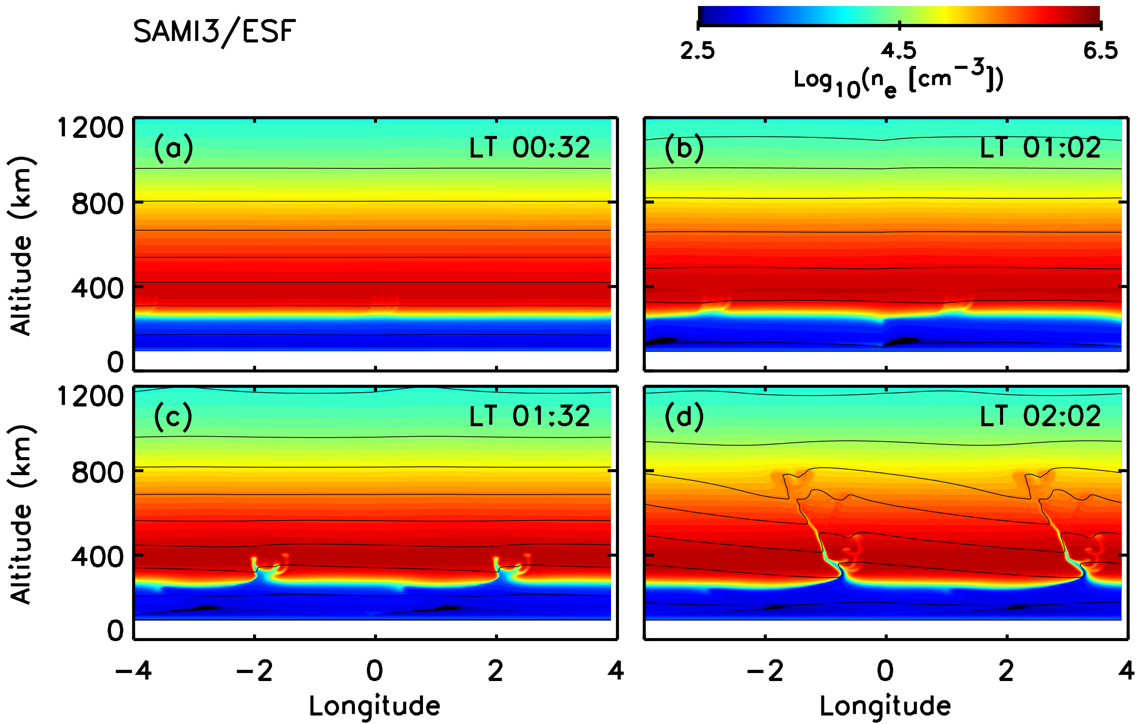

SAMI3/ESF
2.5
4.5
6.5
$\mathrm{Log}_{10}(n_e\ [\mathrm{cm}^{-3}])$
(a)
LT 00:32
(b)
LT 01:02
(c)
LT 01:32
(d)
LT 02:02
Altitude (km)
1200
800
400
0
Longitude
-4
-2
0
2
4

Figure 5.

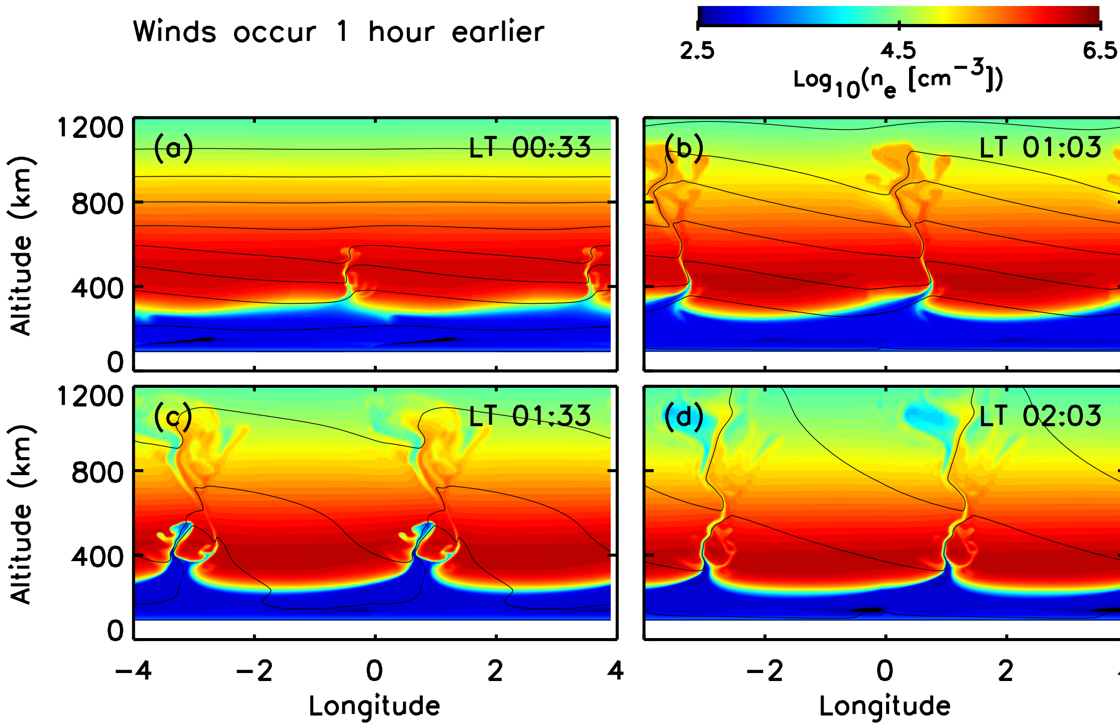

Winds occur 1 hour earlier
2.5
4.5
6.5
Log10(ne [cm−3])
(a)
LT 00:33
(b)
LT 01:03
(c)
LT 01:33
(d)
LT 02:03
Altitude (km)
1200
800
400
0
−4
−2
0
2
4
Longitude

Figure 6.

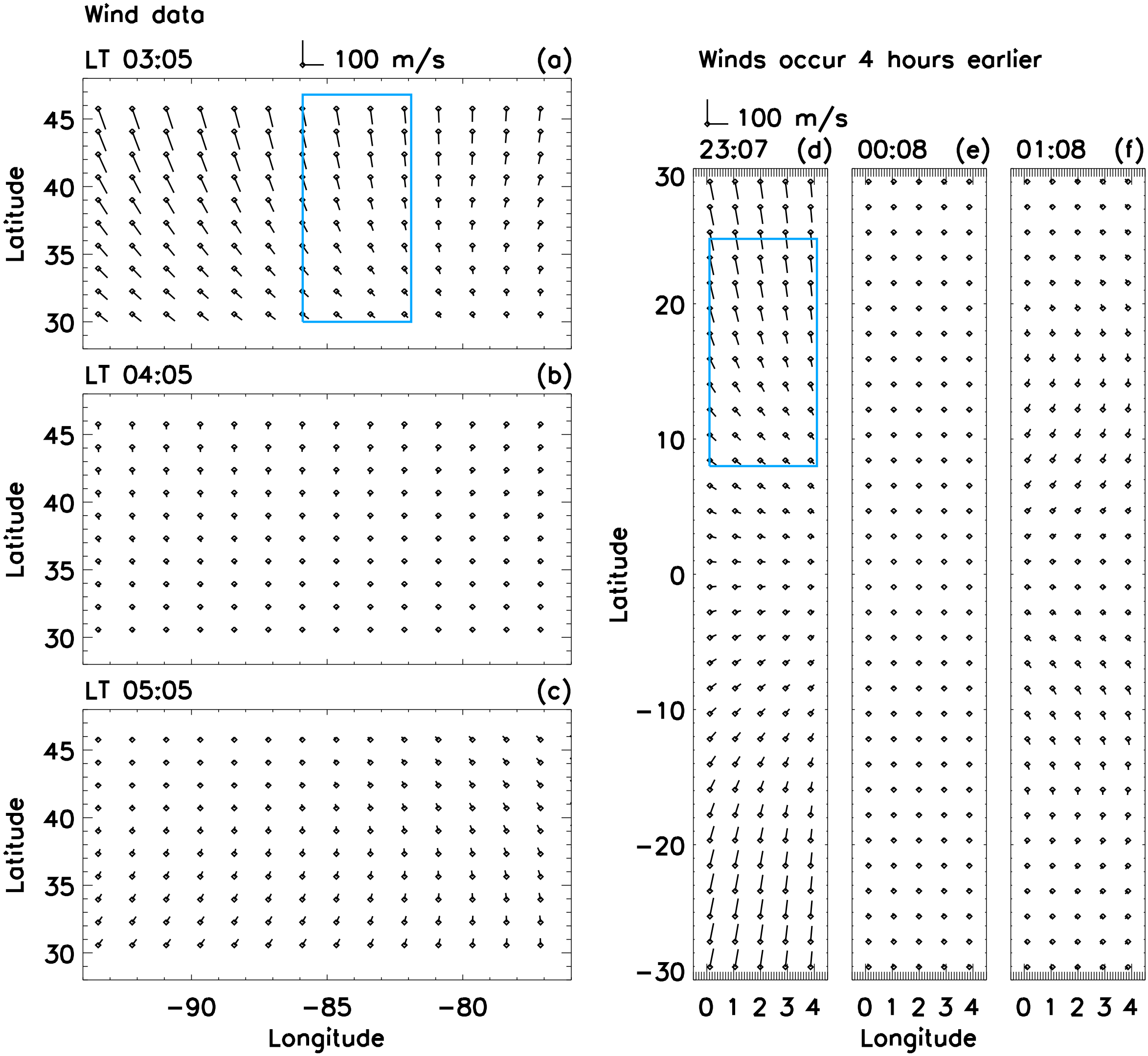
Wind data
LT 03:05
100 m/s
(a)
LT 04:05
(b)
LT 05:05
(c)
Latitude
Longitude
Winds occur 4 hours earlier
100 m/s
23:07
(d)
00:08
(e)
01:08
(f)
Latitude
Longitude

Figure 7.

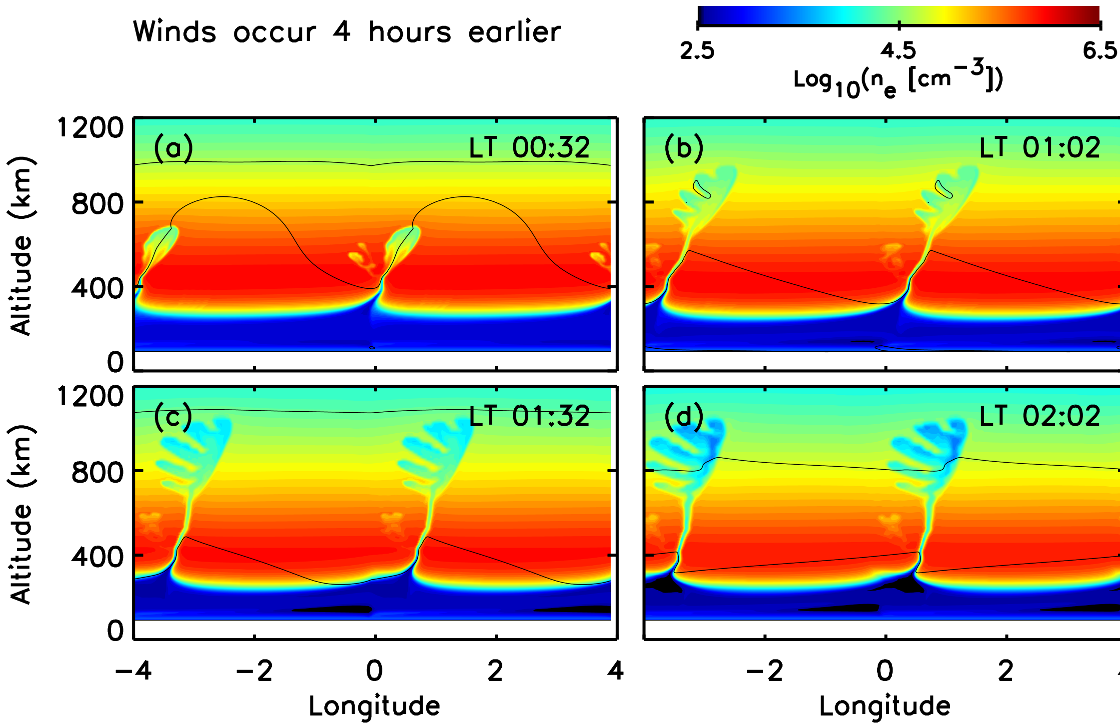

Winds occur 4 hours earlier
2.5
4.5
6.5
Log10(ne [cm−3])
(a)
LT 00:32
(b)
LT 01:02
(c)
LT 01:32
(d)
LT 02:02
Altitude (km)
1200
800
400
0
Altitude (km)
1200
800
400
0
−4
−2
0
2
4
Longitude
−2
0
2
4
Longitude

Figure 8.

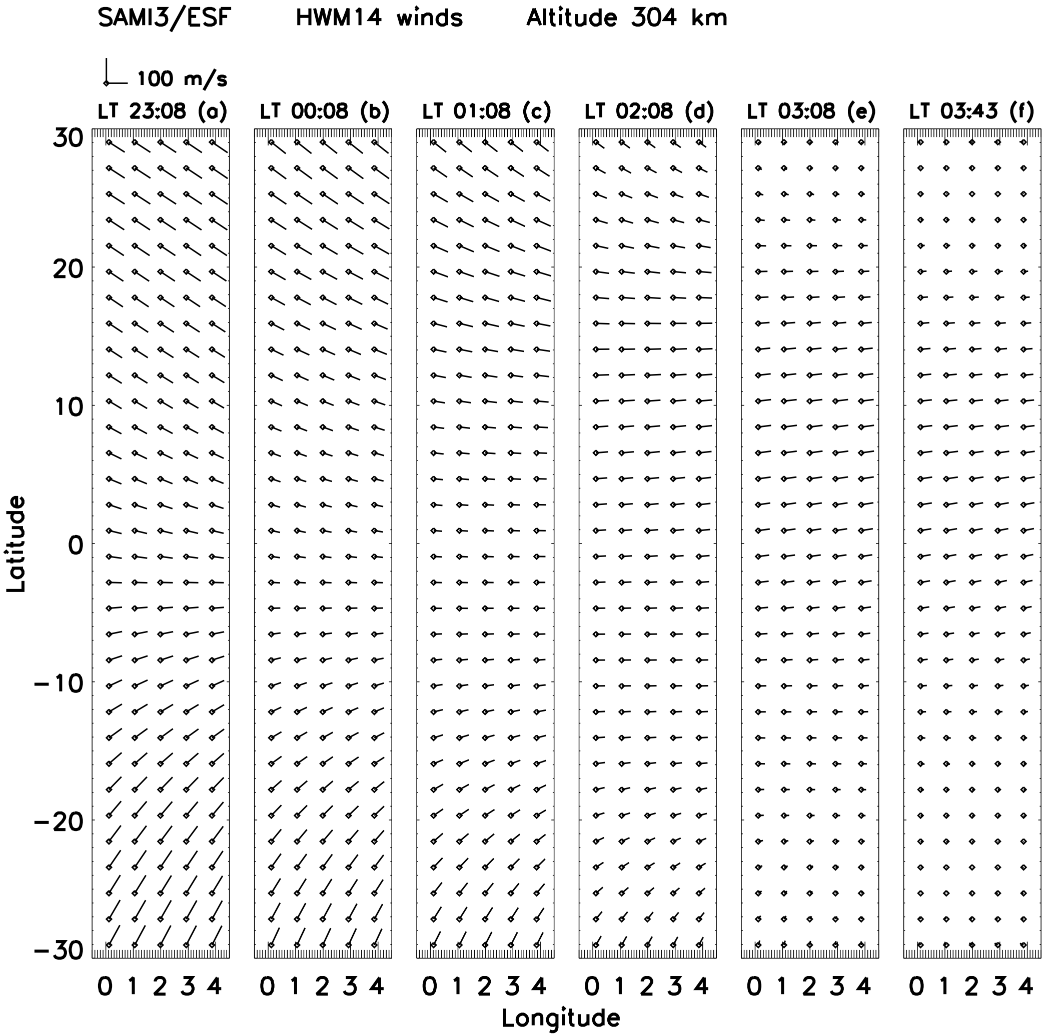

SAMI3/ESF HWM14 winds Altitude 304 km
100 m/s
LT 23:08 (a)
LT 00:08 (b)
LT 01:08 (c)
LT 02:08 (d)
LT 03:08 (e)
LT 03:43 (f)
Latitude
30
20
10
0
−10
−20
−30
0 1 2 3 4
Longitude

Figure 9.

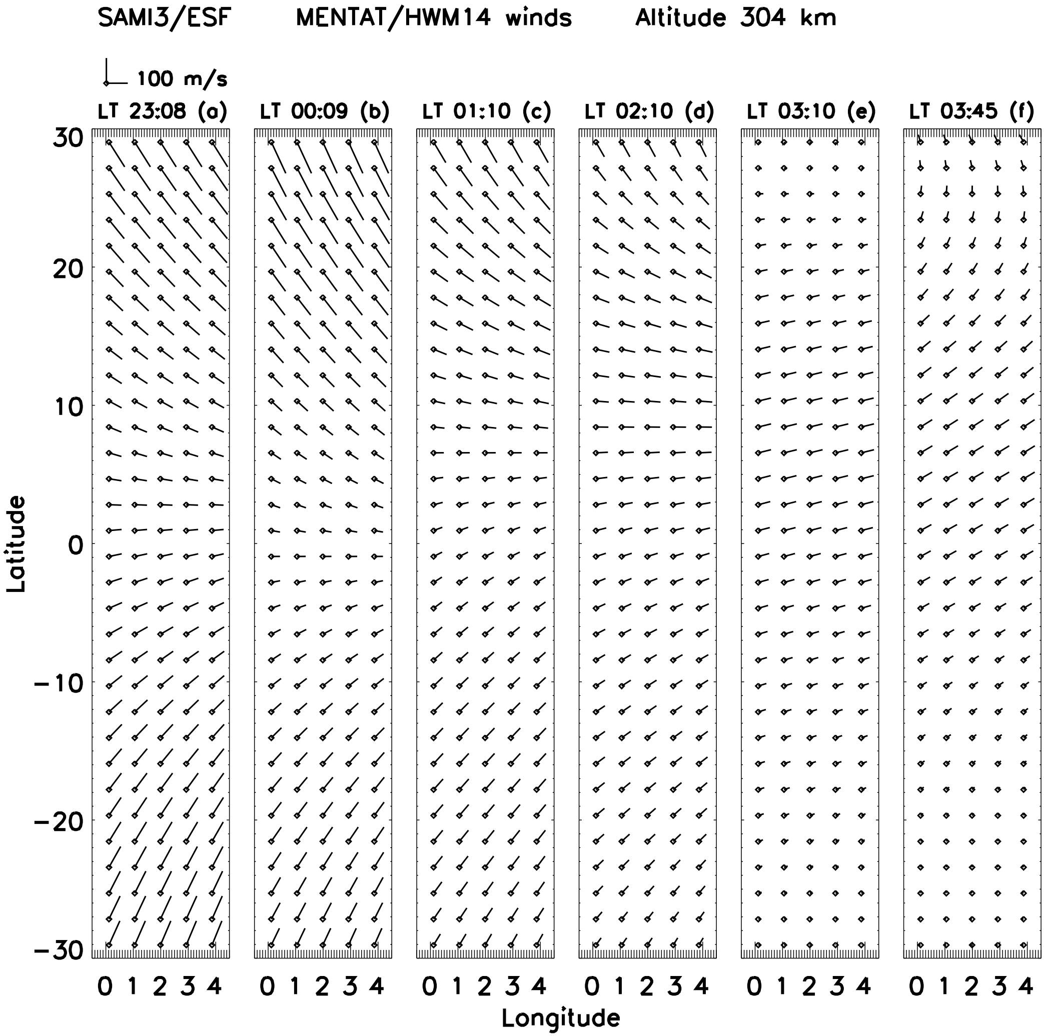
SAMI3/ESF
MENTAT/HWM14 winds
Altitude 304 km
100 m/s
LT 23:08 (a)
LT 00:09 (b)
LT 01:10 (c)
LT 02:10 (d)
LT 03:10 (e)
LT 03:45 (f)
Latitude
30
20
10
0
−10
−20
−30
0 1 2 3 4
Longitude